ARTICLE

Tailoring photodetection performance of self-powered Ga_2O_3 UV solar-blind photodetectors through asymmetric electrodes

Received 00th January 20xx,
Accepted 00th January 20xx

DOI: 10.1039/x0xx00000x

Keyun Gu[a], Zilong Zhang*[b], Haofei Huang[a], Ke Tang[a], Jian Huang*[a,c], Meiyong Liao[b], Linjun Wang[a,c]

Self-powered solar-blind UV detectors have become an increasingly critical role in the sustainable development of photodetectors with low energy consumption. In this work, the design of electrode structures, including the asymmetric-size structure and the asymmetric-material structure, was proposed to achieve the self-powered photodetection function for solar-blind UV a-Ga_2O_3 based photodetectors with the metal-semiconductor-metal (MSM) structure. The results indicate that the Au/Ti/Ga_2O_3/Ti/Au photodetector with the asymmetric-electrode-size hosts photodetection performances of responsivity (*R*), external quantum efficiency (*EQE*) and detectivity (*D**) of 0.149 mA/W, 0.07% and 3.1×10^9 cm $Hz^{1/2}$ W^{-1} @0 V, respectively. The asymmetric-electrode-material photodetectors with Au/Ti/Ga_2O_3/GZO and Au/Ti/Ga_2O_3/Au structures possess photodetection performances of *R*, *EQE*, *D** of 0.591 mA/W, 0.29%, 2.9×10^9 cm $Hz^{1/2}$ W^{-1}, and 0.148 mA/W, 0.07%, 7.8×10^8 cm $Hz^{1/2}$ W^{-1} @0 V, respectively. The electrodes with the asymmetric-size structure and the asymmetric-material structure result in difference Schottky barrier heights in interfaces of electrodes and films, which are in favor of realizing the self-powered performance. The self-powered solar-blind UV a-Ga_2O_3 based photodetectors have fast photo-response speed, high-stability and high-repeatability. These findings provide a promising and facile route to fabricate a-Ga_2O_3 self-powered solar-blind UV photodetectors with high photodetection.

Introduction

Solar-blind ultraviolet (UV) photodetectors, which work in the wavelength region of 200~280 nm, have attracted an increasing attention in many application fields, such as ultraviolet communication, ultraviolet imaging, biology, and missile warning system due to its excellent properties including high sensitivity, high signal-to-noise ratio, small size, and light weight [1-10]. By using the internal built-in electric field in a junction device, self-powered solar-blind UV photodetectors can be realized since its electron-hole pairs were independently separated by the built-in electric field [11-16]. Nowadays, the smart photodetectors with the merits of high intelligence, high integration, miniaturized size, and low energy cost are in demand, which is favour in the sustainable development and practical application [17]. Compared to other semiconductor materials, such as silicon (Si), diamond, GaN, MgZnO, AlGaN, *etc*., the Ga_2O_3 material is an ideal candidate for fabricating solar blind photodetectors due to its suitable band-gap (~4.9 eV), facile preparation process, and low cost [18-21]. Up to now, various kinds of self-powered UV solar-blind photodetectors based on Ga_2O_3 materials grown on different substrates have been reported, which include the device structures of p-n junctions, heterojunctions and Schottky junctions. Guo et al. [22] investigated the photodetection performance of a p-n junction detector based on the structure of GaN/Sn:Ga_2O_3 on sapphire substrate. It exhibited a high performance of responsivity, *R* up to 3.05 A/W under the 254 nm illumination @ 0 V. Wang et al. [23] fabricated an all-oxide NiO/Ga_2O_3 solar-blind photodetector with the p-n junction structure, which hosts a responsivity of 57 μA/W @ 0 V when exposed to a 254 nm light source. He et al. [24] manufactured a α-Ga_2O_3/Cu_2O p-n junction for a UV photodetector, which exhibited a *R* of 0.42 mA/W under 254 nm UV light @ 0 V. Zhao et al. [15] fabricated a single ZnO-Ga_2O_3 self-powered photodetector with a core-shell heterostructure with the responsivity of 9.7 mA/W under 251 nm UV light @ 0 V. Alternatively, Chen et al. [16] reported that the Au/β-Ga_2O_3 nanowire array with a Schottky junction structure exhibited high response speed. Zhi et al. [25] reported a planar Au/β-Ga_2O_3 solar blind photodetector with a Schottky junction structure, which displayed a *R* of 0.4 mA/W and a fast response time (τ_d=50 ms). Nevertheless, the preparation process of crystalline Ga_2O_3 materials and the doping of Ga_2O_3 materials need high growth temperatures and are limited to certain substrates.

Compared with the vertical structure devices including p-n junctions, heterojunctions and Schottky junctions, the planar asymmetric photodetector based on the Schottky junction with metal-semiconductors-metal (MSM) topography has advantages of simple fabrication process, low cost, and high collection efficiency of carriers[26, 27]. The self-power characteristics of solar blind photodetectors can be realized by adjusting electrode sizes and electrode materials on MSM device structures. In our previous work, we fabricated β-Ga_2O_3 and amorphous Ga_2O_3 (a-Ga_2O_3) based photodetectors [28, 29]. The fabrication process of a-Ga_2O_3 through the RF sputtering system is facile, which is in favor of the large-area scale fabrication and the batch in production. Up to now, few reports focus on self-powered MSM UV solar-blind photodetectors based on a-Ga_2O_3 materials. In this work, we fabricated MSM solar-blind photodetectors based on a-Ga_2O_3 films grown on Si substrates by tailoring electrode sizes and electrodes materials, respectively. The Ga doped ZnO (GZO) material has excellent transparency and conductivity, which exhibits a bright potential in regarding as the electrode for the Ga_2O_3-based photodetector. The UV solar-blind

[a] *School of Materials Science and Engineering, Shanghai University, Shanghai 200444, PR China.*
Email: jianhuang@shu.edu.cn
[b] *Research Center for Functional Materials, National Institute for Materials Science (NIMS), Namiki 1-1, Tsukuba, Ibaraki 305-0044, Japan.*
Email: zlzhang16@hotmail.com or ZHANG.Zilong@nims.go.jp
[c] *Zhejiang Institute of Advanced Materials, SHU, Jiashan 314113, PR China.*
† Electronic Supplementary Information (ESI) available. See DOI: 10.1039/x0xx00000x

photodetectors based on the asymmetric electrode size (Au/Ti/Ga_2O_3/Ti/Au) and the asymmetric electrode material (Au/Ti/Ga_2O_3/GaZnO (GZO) and Au/Ti/Ga_2O_3/Au) show good response to 254 nm UV illumination at 0 V bias voltage. This work demonstrates an effective approach for realizing the self-powered detection performance of a-Ga_2O_3 based photodetectors, showing a promising prospective to make the miniaturized and high-integrated UV solar-blind photodetectors with other semiconductor devices for the practical applications.

Results and discussion

Figure. 1(a) displays a XRD pattern of a typical Ga_2O_3 film grown on Si substrate at RT. There is no existence of diffraction peak associated with the crystalline Ga_2O_3 film except for those of the Si substrate, which indicates that the as-grown Ga_2O_3 film is amorphous structure. To investigate the surface property of Ga_2O_3 film, we conducted the AFM test on 2 μm×2 μm area of the Ga_2O_3 film, as shown in Fig. 1(b). The surface exhibits uniform distribution of grains with the root mean square (RMS) of around 7.325 nm. Fig. 1(c-d) exhibit the X-ray photoelectron spectroscopy (XPS) results. It indicates two peaks appear around 1118.4 eV and 1145.5 eV, which corresponds to Ga $2p_{3/2}$ and Ga $2p_{1/2}$, respectively. The O 1s core-level spectrum is fitted into two components: one peak of O Ⅰ (around 530.8 eV) and the other peak of OⅡ (around 531.8 eV). The later peak originates from O^{2-} ions in oxygen-deficient regions [5, 30]. The peak area represents the proportion of the corresponding component. In Fig. 1(d), the peak area of OⅡ is larger than that of O Ⅰ, indicating that there are many oxygen vacancies existed in the Ga_2O_3 film. Furthermore, the ratio of O/Ga is calculated as 0.818 according to the peak intensities of Ga $2p_{3/2}$ and O 1s while the theoretical ratio of O/Ga is 1.5. It further confirms that there are high oxygen concentrations in a-Ga_2O_3 films. These results agree with the findings of other researches [31, 32].

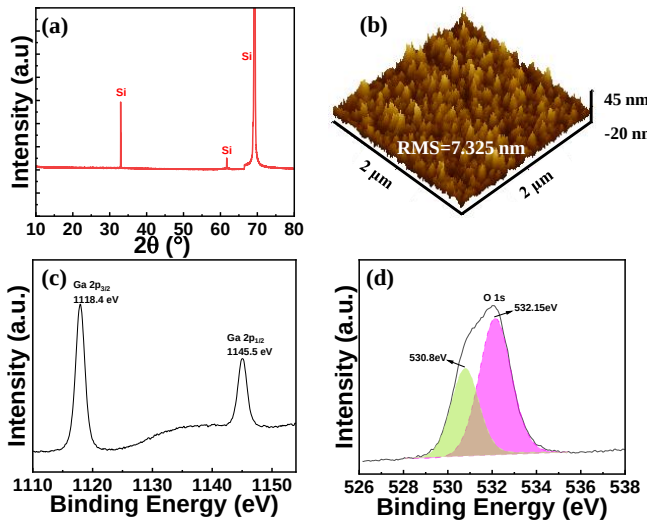

Fig. 1. (a) XRD spectrum, (b) AFM image and XPS spectrum, (c) Ga 2p, (d) O 1s of a Ga_2O_3 thin film grown on Si substrate at RT.

The *I-V* characteristics of a-Ga_2O_3-based photodetectors with the symmetric-electrode-size and the asymmetric-electrode-size were measured through the Keithley 4200/SCS facility. Fig. 2(a) and (c) schematically show the photodetection measurement setup of these two kinds of photodetectors. The dark-current, I_d and photo-current, I_p of the photodetector was measured in the dark condition and under the 254 nm UV light illumination with the intensity of 120 μW/cm^2, respectively. As shown in Fig. 2(b) and (d), the dependences of I_d on the applying voltage of the symmetric-electrode-size detector have highly symmetrical characteristic. The I_d of the a-Ga_2O_3-based photodetector with the symmetric-electrode-size structure is almost equal to I_p at 0 V bias, which displays it exhibits no response to the 254 nm UV light illumination without an external power supply. This result is similar to other works [33-35]. However, the I_p of the a-Ga_2O_3-based photodetector with the asymmetric-electrode-size structure is higher than I_d at 0 V bias, which demonstrates this detector realizes a photo-response to the 254 nm UV light illumination without an external power supply. The responsivity (*R*), external quantum efficiency (*EQE*), and detectivity (*D**) are critical parameters to evaluate the photodetection performance of photodetectors. These parameters can be expressed as follows [36]:

$$\boldsymbol{R} = \frac{\boldsymbol{I_p - I_d}}{\boldsymbol{P}} \quad (1)$$

$$\boldsymbol{EQE} = \frac{\boldsymbol{hc}}{\boldsymbol{e\lambda}}\boldsymbol{R} \quad (2)$$

Wherein *P* is the light power intensity, *h* is the Planck's constant, *c* is the speed of light, *e* is the electronic charge, and λ is the wavelength of incident light. The detectivity *D** of a photodetector is used to evaluate the noise, as defined to be [37-40]

$$D^* = \frac{R(A\Delta f)^{1/2}}{I_n} \quad (3)$$

where *R* is the responsivity of photodetector. *A* is the effective illumination area of detector, Δf is the bandwidth, and I_n is the current noise mainly caused by carrier generation and recombination processes. There are three main contributions to the noise that limits D*, including dark-current-induced shot noise, Johnson-Nyquist noise, and thermal fluctuation "flicker" noise. If, as expected, the shot noise from the dark current is the major contribution. Thus, the detectivity can be simplified as [37, 38]

$$\boldsymbol{D^*} = \boldsymbol{R}\sqrt{\frac{\boldsymbol{A}}{\boldsymbol{2eI_d}}} \quad (4)$$

Based on these above equations, the *R*, *EQE*, and *D** were calculated as shown in table 1. At 0 V bias, the *R*, *EQE* and *D** are 0.149 mA/W, 0.07% and 3.1×10^9, respectively. Fig. 2(e) shows the transient response of the a-Ga_2O_3-based photodetector with the asymmetric-electrode-size structure. It depicts that the I_p intensively increases to a stable value with the UV light turn-on and rapidly decreases with the UV light turn-off. In addition, after several measurement cycles, the photodetection performance of this photodetector shows weak change, indicating a good stability. Fig. 2(f) is the enlarged view of one cycle for the transient response test. It exhibits that the rise time (τ_r, the time for the current increasing from 10% to 90% of the maximum photocurrent) is 0.759 s and the decay time (τ_d, the time for the current decreasing from 90% to 10% of the maximum photocurrent) is 0.451 s. Besides, the a-Ga_2O_3-based photodetector with the asymmetric-electrode-size structure has the good stability of photodetection performance as kept in atmosphere for two months (Fig. S1 (a), Supplementary data).

Table 1. Photodetection performance of the a-Ga_2O_3-based photodetector with the asymmetric-electrode-size structure

Voltage (V)	*R* (mA/W)	*EQE* (%)	*D** (cm Hz$^{1/2}$ W^{-1})	τ_r/τ_d (s)
0	0.149	0.07	3.1×10^9	0.759/0.451

Figure 3(a-c) show the energy band diagrams of the a-Ga_2O_3-based photodetector with the symmetric electrode structure in the dark condition and under the 254 nm UV light illumination at 0 V bias. The thermionic emissions expressed by Eq. (5) was used to calculate the height of the Schottky barrier height [41-44].

$$J_s = A^* T^2 \, exp(-q\phi_B/kT) \quad (5)$$

Where k is Boltzmann's constant, T is the evaluated temperature, e is the electron charge, J_s is the saturation current density of the device and it can be obtained from the fitting line intercept of ln$J$-V, which is shown in Fig. S2. A^* is the Richardson constant, which was estimated as 41 A·cm^{-2}·K^{-2} [45]. According to the calculation, the heights of the Schottky barrier height between Au/Ti electrode and Ga_2O_3 film on both sides are 0.880 eV and 0.879 eV, respectively, indicating the height of the Schottky barriers on both sides are almost equal. As shown in Fig. 3(a), due to a relatively higher Schottky barrier, few electrons can cross the interface between the Ga_2O_3 film and the electrode, which results in a limited current in the dark current. Under the 254 nm UV light illumination, the photo electron-hole pairs are generated and moved by a built-in electric field. The photogenerated electrons move away from the contact in the conduction band while the holes move towards the contact interface between the metal electrode and the Ga_2O_3 film, as shown in Fig. 3(b). Many defect states like oxygen deficiency existed at the contact interface can capture photogenerated holes, resulting in a decreased Schottky barrier height [46-51]. Since the electrode width of Au/Ti-1 is larger than that of Au/Ti-2, the number of photogenerated holes captured by Au/Ti-1 is more than that of Au/Ti-2, which leads to a difference Schottky barrier height in the interfaces of Au/Ti-1 electrode and Au/Ti-2 electrode (Fig. 3(c)). In the absence of external power supply, the photogenerated electrons can drift from the Au/Ti-2 side to the Au/Ti-1 side, realizing the self-powered photodetection performance.

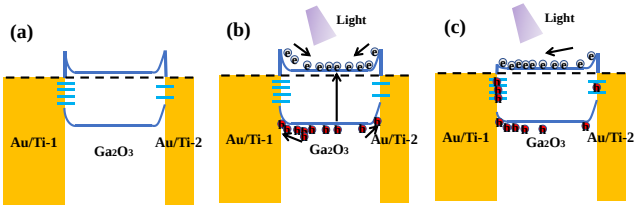

Fig. 3. Schematic diagrams of the energy band of a self-powered photodetector with the asymmetrical electrode size under various conditions: (a) in the dark condition and (b), (c) under the UV light illumination.

As for the photodetector with the Au/Ti/Ga_2O_3/GZO structure (called Au/Ti/Ga_2O_3/GZO photodetector), the positive electrode of the semiconductor analyzer probe is connected to the GZO electrode side and the negative electrode is connected to the Au/Ti side, as shown in Fig. 4(a). As for the photodetector with the Au/Ti/Ga_2O_3/Au structure (called Au/Ti/Ga_2O_3/Au photodetector), the positive electrode of the semiconductor analyzer probe is connected to the Au/Ti electrode side and the negative electrode is connected to the Au side, as shown in Fig. 4(e). Fig. 4(b) and (f) shows the measured plots of I-V characteristics under the dark condition and the light illumination, it can be seen that the I_d of these two photodetectors is obviously asymmetric, and the I_p are higher than the I_d at 0 V bias, which reveals these photodetectors exhibit good respond to the 254 nm UV light illumination in the absence of external power supply. When the UV light source is turned on, the current rises rapidly, and when the UV light source is turned off, the current decreases fast at 0 V bias (Fig. 4(c) and (g)). Moreover, these two photodetectors have high stability and repeatability of photodetection performances. Furthermore, these Au/Ti/Ga_2O_3/GZO and Au/Ti/Ga_2O_3/Au photodetectors host the overshooting performance of I_p with the light turn-on. It means that the I_p suddenly rises to a high value and then gradually decreases to a stable value as the UV light source is turned on. This is attributed that the photogenerated carriers increase instantaneously with the UV light turn-on. Since there is no external power supply, the built-in electric field is not enough to continuously drive the transmission of photogenerated carriers, which results in the carrier accumulation. Thus, the I_p instantaneously increases. Then, the photogenerated carriers are reduced by the recombination until the I_p decays to a stable value [52, 53]. From Fig. 4(d) and (h), we obtained that τ_r/τ_d of Au/Ti/Ga_2O_3/GZO and Au/Ti/Ga_2O_3/Au photodetectors are 1.060 s/0.342 s and 0.091 s/0.073 s, respectively. According to Eqs. (1), (2) and (3), the R, EQE,

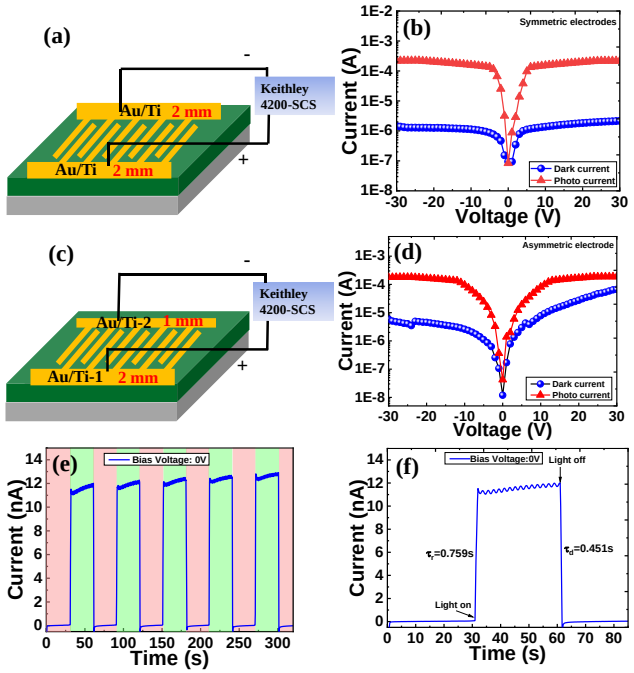

Fig. 2. (a) and (c) Schematic measurement setups of a-Ga_2O_3-based photodetectors with the symmetric electrode structure and the asymmetric electrode structure. (b) and (d) I-V curves of these two photodetectors measured under the dark condition and the 254 nm UV light illumination. (e) Time-dependent photo response of the a-Ga_2O_3-based photodetector with the asymmetric-electrode-size structure @ 0 V, (f) Amplified curve of one test cycle for the rise and decay process @ 0 V.

Table 2. Photodetection performances of a-Ga2O3 photodetectors with asymmetric-electrode-material structures

Photodetector type	Voltage (V)	R (mA/W)	EQE (%)	D^* (cm Hz$^{1/2}$ W^{-1})	τ_r/τ_d (s)
Au/Ti/Ga_2O_3/GZO	0	0.591	0.29	2.9×10^9	1.060/0.342
Au/Ti/Ga_2O_3/Au	0	0.148	0.07	7.8×10^8	0.091/0.073

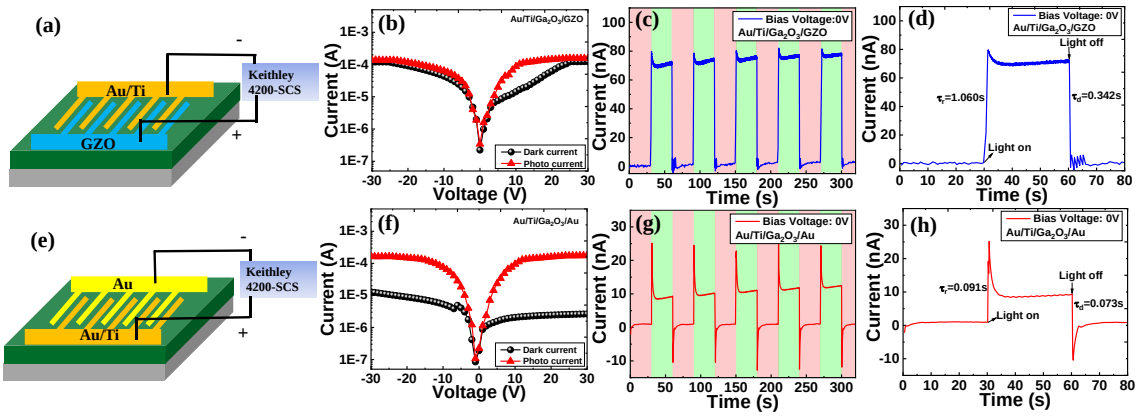

Fig. 4. (a) and (e) Schematic setup diagrams of photodetectors with Au/Ti/Ga_2O_3/GZO and Au/Ti/Ga_2O_3/Au structures. (b) and (f) *I-V* plots measured under the dark condition and the 254 nm UV light illumination. (c) and (g) Dependences of I_p on the test time. (d) and (h) One-cycle measured curves of the current rise and decay process.

and D^* of Au/Ti/Ga_2O_3/GZO and Au/Ti/Ga_2O_3/Au photodetectors are calculated as 0.591 mA/W, 0.29%, 2.9×10^9 cm $Hz^{1/2}$ W^{-1} and 0.148 mA/W, 0.07%, 7.8×10^8 cm $Hz^{1/2}$ W^{-1}, respectively, as shown in Table 2. The oxygen vacancies in detectors with asymmetric electrode materials exhibit weak influence on the photodetection performance due to no variation in the electrode size dimension. Alternatively, these Au/Ti/Ga_2O_3/GZO and Au/Ti/Ga_2O_3/Au photodetectors have outstanding stability and repeatability of photodetection performances after placed in atmosphere two months as shown in Fig. S1 (b) and (c).

From Figure. S3 and Eq. (4), the height of Schottky barrier, $q\Phi_{B1}$ between the Ga_2O_3 and the Au/Ti, the $q\Phi_{B2}$ between the Ga_2O_3 and the GZO, and the $q\Phi_{B3}$ between the Ga_2O_3 and the Au are calculated as 0.880 eV, 0.863 eV and 0.898 eV, respectively. As displayed in Fig. 5, few electrons are existed in the dark condition, while under the 254 nm UV light illumination, more electrons are generated. For the Au/Ti/Ga_2O_3/GZO photodetector, as-photogenerated electrons drift from the Au/Ti electrode with the high Schottky barrier height to the GZO electrode with the low Schottky barrier height. For the Au/Ti/Ga_2O_3/Au photodetector, as-photogenerated electrons move from the Au electrode to the Au/Ti electrode. Thus, these photodetectors with asymmetric-electrode-material structures realize the self-powered photodetection performance.

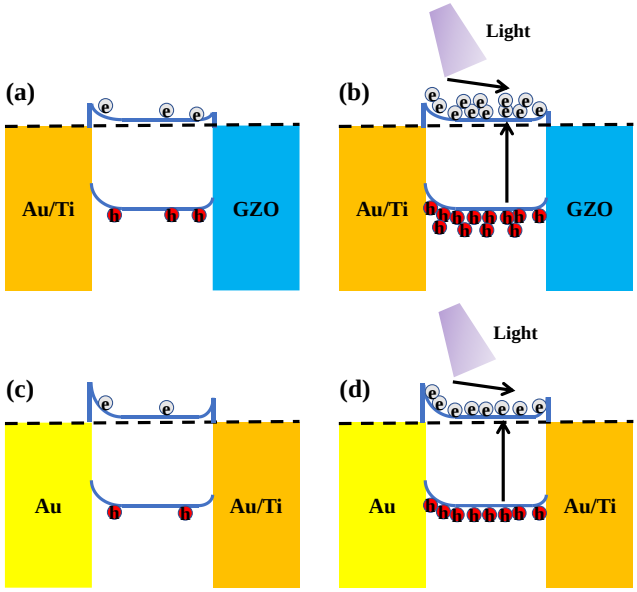

Fig. 5. Schematic diagrams of the energy bands of a-Ga_2O_3 based photodetectors with asymmetrical electrode material structures: (a) in the dark condition and (b) under the UV light illumination for the Au/Ti/Ga_2O_3/GZO photodetector. (c) in the dark condition and (d) under the UV light illumination for the Au/Ti/Ga_2O_3/Au photodetector.

The comparisons of photodetection performances of Ga_2O_3-based self-powered photodetectors are shown in Table 3. The self-powered photodetectors in this work have better responsivity performance. Furthermore, compared to other photodetectors with complex structure based on the crystalline Ga_2O_3, self-powered photodetectors in this work exhibit facile fabrication process, simple structure, which have enormous potential to realize high integration and miniaturization with other electronics for the photodetection applications. In addition, in our future work, the photodetection performance of the self-power a-Ga_2O_3 photodetector can be enhanced through 1) the improvement in quality of the a-Ga_2O_3 thin film; 2) the optimization structures of asymmetric electrodes. Furthermore, the XPS and ultraviolet photoelectron spectroscopy (UPS) studies are critical for getting a better understanding of interfaces from metal electrodes to Ga_2O_3 films. The interface studies between various metals and Ga_2O_3 thin films will be performed in details in our future work, main including influences of various mechanical/chemical surface polishing and the metal kinds on the interface contact. The XPS and UPS techniques will be utilized in details to analyze interface states.

Table 3. Comparisons of photodetection performances of Ga_2O_3-based photodetectors.

Materials	Structure	Growth method	R	τ_r/τ_d	Ref
a-Ga_2O_3	NiO/Ga_2O_3 p–n junction	RF	57 μA/W@0 V	0.34/3.65 s	23
β-Ga_2O_3	Au/β-Ga_2O_3 Schottky Junction	-	0.01 mA/W@0 V	~1×10^{-6}/~6×10^{-5} s	16
β-Ga_2O_3	β-Ga_2O_3/4H-SiC heterojunction	PLD	10.35 mA/W@0 V	11 ms/19 ms	54
ZnO-Ga_2O_3 core–shell	ZnO-Ga_2O_3 heterojunction	One-step CVD	9.7 mA/W@0 V	100 μs/900 μs	15
Doped β-Ga_2O_3	VO_x/Ga_2O_3 heterojunction	MOCVD	28.9 mA/W@0 V	57 ms/74 ms	55
a-Ga_2O_3	Au/Ti/Ga_2O_3/Ti/Au MSM	RF	0.149 mA/W@0 V	0.759 s/0.451 s	This work
a-Ga_2O_3	Au/Ti/Ga_2O_3/GZO MSM	RF	0.591 mA/W@0 V	1.060 s/0.342 s	This work
a-Ga_2O_3	Au/Ti/Ga_2O_3/Au MSM	RF	0.148 mA/W@0 V	0.091 s/0.073 s	This work
β-Ga_2O_3	Ni/Au/β-Ga_2O_3/Ti/Au	MBE	1.4 mA/W@0 V	1.1 s/0.3 s	56
β-Ga_2O_3	diamond/β-Ga_2O_3 heterojunction	PECVD	0.2 mA/W@0 V	-	57
β-Ga_2O_3	$CuMO_2$/Ga_2O_3 pn heterojunction	MOCVD	0.025 mA/W@0 V	0.26 s/0.14 s	58
α-Ga_2O_3	Ga_2O_3-Al_2O_3 nano tree	-	0.174 mA/W@0 V	0.1 s/0.1 s	59

Experimental

High-quality a-Ga_2O_3 films were grown on (100)-Si substrates by using a RF magnetron sputtering system. The growth parameters are as follows: the substrate temperature of room temperature (RT), the sputtering power of 200 W, the work pressure of 20 mTorr, the atmosphere of 100% Ar, the growth duration of 4 h. The thickness of the as-grown a-Ga_2O_3 film is about 400 nm. The substrate temperature was measured through the thermocouple (CuNi), exhibiting a tiny variation in the substrate temperature during the film growth. X-ray diffraction (XRD) test and atomic force microscope (AFM) facilities were utilized to check amorphous properties and measure surface morphologies of the Ga_2O_3 films, respectively. The XPS technique was utilized to observe the oxygen vacancy concentration in a-Ga_2O_3 films. Prior to electrode depositions, Ga_2O_3 films were orderly ultrasonic cleaned in deionized water, acetone, ethanol, and deionized water for 5 minutes, respectively. The electrodes of 20 nm Ti and 80 nm Au were deposited on a-Ga_2O_3 films at a rate of 0.5 Å/s by using an electron beam deposition facility. The electrodes of GZO films were deposited on a-Ga_2O_3 films through a RF magnetron sputtering system. As for an asymmetric-electrode-size detector, the width of one side electrode of Au/Ti-1 was set as 2 mm and the other side electrode of Au/Ti-2 was set as 1 mm. For the comparison of photodetection performance, we also fabricated a detector with a symmetrical electrode size of 2 mm in width. For the fabrication of an asymmetric-electrode-material detector (Au/Ti/Ga_2O_3/GZO), a 100 nm-thick GZO electrode was deposited on one side of a-Ga_2O_3 film. Then, the 20 nm-thick Ti film followed by an 80 nm-thick Au film was deposited on the other side of a-Ga_2O_3 films. In the same way, in order to fabricate the Au/Ti/Ga_2O_3/Au photodetector, 20 nm Ti and 80 nm Au were deposited as one side of the interdigital electrode. And then, the other side of the Au electrode with a thickness of 100 nm was deposited. The interfinger spacing is the same for all detectors. A Keithley 4200/SCS semiconductor characterization system and a ZF-5 UV light source (120 μW) were applied to measure the optical detection performance of a-Ga_2O_3 based UV solar-blind detectors. The distance between the light source and the sample is about 2 cm. In order to avoid the photo-response from the GZO electrode, the wavelength of ZF-5 UV light source of 254 nm is utilized to examine the photodetection performance of detectors.

Conclusions

In summary, the self-powered asymmetric-electrode-size photodetector and asymmetric-electrode-material photodetector based on amorphous Ga_2O_3 films grown on Si substrates were fabricated, respectively. The self-powered photodetection function was realized through the electrode design of asymmetric-size and asymmetric-material. For the asymmetric-electrode-size photodetector, it hosts photodetection performances of *R*, *EQE* and *D** of 0.149 mA/W, 0.07% and 3.1×10^9 @0 V, respectively. The asymmetric-electrode-material photodetectors with the Au/Ti/Ga_2O_3/GZO structure and the Au/Ti/Ga_2O_3/Au structure possess photodetection performances of *R*, *EQE*, *D** of 0.591 mA/W, 0.29%, 2.9×10^9 cm $Hz^{1/2}$ W^{-1}, and 0.148 mA/W, 0.07%, 7.8×10^8 cm $Hz^{1/2}$ W^{-1} @0 V, respectively. Besides, detectors with asymmetric electrodes including the asymmetric-size structure and the asymmetric-material structure have the fast photo-response speed under the 254 nm UV light illumination without an external energy supply. These results reveal the excellent self-powered photodetection performances of a-Ga_2O_3 based photodetectors with MSM structures are tailored by modulating asymmetric electrodes. This work provides a promising and facile strategy for fabricating self-powered a-Ga_2O_3 based solar-blind UV photodetectors with high photodetection performance.

Conflicts of interest

The authors declare that they have no conflict of interest.

Acknowledgements

This work was funded by the National Natural Science Foundation of China (No. 11875186).

Notes and references

1. T. Oshima, T. Okuno, N. Arai, N. Suzuki, H. Hino and S. Fujita, *Jpn. J. Appl. Phys.*, 2009, **48**, 011605.
2. F. Omnès, E. Monroy, E. Muñoz and J.-L. Reverchon, 2007.
3. L. Li, P. S. Lee, C. Yan, T. Zhai, X. Fang, M. Liao, Y. Koide, Y. Bando and D. Golberg, *Adv. Mater.*, 2010, **22**, 5145-5149.
4. H. Chen, H. Liu, Z. Zhang, K. Hu and X. Fang, *Adv. Mater.*, 2016, **28**, 403-433.
5. D. Guo, Z. Wu, Y. An, X. Guo, X. Chu, C. Sun, L. Li, P. Li and W. Tang, *Appl. Phys. Lett.*, 2014, **105**, 023507.
6. H. Chen, K. Liu, L. Hu, A. A. Al-Ghamdi and X. Fang, *Mater. Today*, 2015, **18**, 493-502.
7. M. Razeghi, *Proceedings of the IEEE*, 2002, **90**, 1006-1014.
8. H. Chen, P. Yu, Z. Zhang, F. Teng, L. Zheng, K. Hu and X. Fang, *Small*, 2016, **12**, 5809-5816.
9. W. Song, J. Chen, Z. Li and X. Fang, *Adv. Mater.*, 2021, **33**, 2101059.
10. M. Liao, *Funtional Diamond,* 2022, **1**, 29-46.
11. Y. Wang, L. Li, H. Wang, L. Su, H. Chen, W. Bian, J. Ma, B. Li, Z. Liu and A. Shen, *Nanoscale*, 2020, **12**, 1406-1413.
12. H. Wang, H. Chen, L. Li, Y. Wang, L. Su, W. Bian, B. Li and X. Fang, *J. Phys. Chem. Lett.*, 2019, **10**, 6850-6856.
13. S. Luan, L. Dong, X. Ma and R. Jia, *J. Alloy. Compd.*, 2020, **812**, 152026.
14. F. Bai, J. Qi, F. Li, Y. Fang, W. Han, H. Wu and Y. Zhang, *Adv. Funct. Mater. Interfaces*, 2018, **5**, 1701275.
15. B. Zhao, F. Wang, H. Chen, L. Zheng, L. Su, D. Zhao and X. Fang, *Adv. Funct. Mater.*, 2017, **27**, 1700264.
16. X. Chen, K. Liu, Z. Zhang, C. Wang, B. Li, H. Zhao, D. Zhao and D. Shen, *ACS Appl. Mater. Interfaces*, 2016, **8**, 4185-4191.
17. C. Sun, M. T. Wade, Y. Lee, J. S. Orcutt, L. Alloatti, M. S. Georgas, A. S. Waterman, J. M. Shainline, R. R. Avizienis and S. Lin, *Nature*, 2015, **528**, 534-538.
18. M. Higashiwaki, K. Sasaki, A. Kuramadta, T. Masui and S. Yamakoshi, *Phys. Status Solidi (a)*, 2014, **211**, 21-26.
19. Y. Chen, Y. Lu, M. Liao, Y. Tian, Q. Liu, C. Gao, X. Yang and C. Shan, *Adv. Funct. Mater.,* 2019, **29**, 1906040.
20. Y. Chen, X. Yang, Y. Zhang, X. Chen, J. Sun, Z. Xu, K. Li, L. Dong and C. Shan, *Nano Res.*, 2022, 1-9.
21. Y. Hao, J. Semicond., 2019, **40**, 010301.
22. D. Guo, Y. Su, H. Shi, P. Li, N. Zhao, J. Ye, S. Wang, A. Liu, Z. Chen and C. Li, *Acs Nano*, 2018, **12**, 12827-12835.
23. Y. Wang, C. Wu, D. Guo, P. Li, S. Wang, A. Liu, C. Li, F. Wu and W. Tang, *ACS Appl. Electron. Mater.*, 2020, **2**, 2032-2038.
24. C. He, D. Guo, K. Chen, S. Wang, J. Shen, N. Zhao, A. Liu, Y. Zheng, P. Li and Z. Wu, *ACS Appl. Nano Mater.*, 2019, **2**, 4095-4103.
25. Y. Zhi, Z. Liu, X. Chu, S. Li, Z. Yan, X. Wang, Y. Huang, J. Wang, Z. Wu and D. Guo, *ECS J. Solid State Sci. Technol.*, 2020, **9**, 065011.
26. S. Wemple, *Phys. Rev. B*, 1970, **2**, 2679.
27. T. N. Bhat, B. Pandey and S. Krupanidhi, *J. Phys. D Appl. Phys.*, 2017, **50**, 275101.
28. K. Gu, Z. Zhang, K. Tang, J. Huang, M. Liao and L. Wang, *Appl. Surf. Sci.*, 2022, **605**, 154606.
29. K. Gu, Z. Zhang, K. Tang, J. Huang, Y. Shang, Y. Shen, M. Liao and L. Wang, *Vacuum*, 2022, **195**, 110671.
30. Y. An, D. Guo, S. Li, Z. Wu, Y. Huang, P. Li, L. Li and W. Tang, *J. Phys. D Appl. Phys.*, 2016, **49**, 285111.
31. M. Heinemann, J. Berry, G. Teeter, T. Unold and D. Ginley, *Appl. Phys. Lett.*, 2016, **108**, 022107.
32. L.-X. Qian, Z.-H. Wu, Y.-Y. Zhang, P. Lai, X.-Z. Liu and Y.-R. Li, *ACS Photonics*, 2017, **4**, 2203-2211.
33. Q. Zheng, F. Huang, K. Ding, J. Huang, D. Chen, Z. Zhan and Z. Lin, *Appl. Phys. Lett.*, 2011, **98**, 221112.
34. D. L. Rogers, *J. Lightwave Technol.*, 1991, **9**, 1635-1638.
35. L. Wang, Z. Ju, J. Zhang, J. Zheng, D. Shen, B. Yao, D. Zhao, Z. Zhang, B. Li and C. Shan, *Appl. Phys. Lett.*, 2009, **95**, 131113.
36. Y. Qin, S. Long, H. Dong, Q. He, G. Jian, Y. Zhang, X. Hou, P. Tan, Z. Zhang and H. Lv, *Chinese Phys. B*, 2019, **28**, 018501.
37. X. Chen, F. Ren, S. Gu and J. Ye, Photonics Res., 2019, **7**, 381-415.
38. X. Gong, M. Tong, Y. Xia, W. Cai, J. S. Moon, Y. Cao, G. Yu, C.-L. Shieh, B. Nilsson and A. Heeger, Science, 2009, **325**, 1665-1667.
39. Y. Wang, Y. Gu, A. Cui, Q. Li, T. He, K. Zhang, Z. Wang, Z. Li, Z. Zhang and P. J. A. M. Wu, *Adv. Mater.,* 2022, **34**, 2107772.
40. A. W. J. O.-E. R. Rogalski, *Opto-Electron. Rev.,* 2022, **30**.
41. D. B. Suyatin, V. Jain, V. A. Nebol'sin, J. Trägårdh, M. E. Messing, J. B. Wagner, O. Persson, R. Timm, A. Mikkelsen and I. Maximov, *Nature Commun.,* 2014, **5**, 1-8.
42. Y. Luo, X. Yan, J. Zhang, B. Li, Y. Wu, Q. Lu, C. Jin, X. Zhang and X. Ren, *Nanoscale*, 2018, **10**, 9212-9217.
43. M. Missous, E. Rhoderick, D. Woolf and S. Wilkes, *Semicond. Sci. Technol.*, 1992, **7**, 218.
44. S. Tongay, M. Lemaitre, X. Miao, B. Gila, B. Appleton and A. Hebard, *Phys. Rev. X*, 2012, **2**, 011002.
45. K. Sasaki, M. Higashiwaki, A. Kuramata, T. Masui and S. Yamakoshi, *IEEE Electr. Device L.*, 2013, **34**, 493-495.
46. L. Su, H. Chen, X. Xu and X. Fang, *Laser Photonics Rev.*, 2017, **11**, 1700222.
47. H.-Y. Chen, K.-W. Liu, X. Chen, Z.-Z. Zhang, M.-M. Fan, M.-M. Jiang, X.-H. Xie, H.-F. Zhao and D.-Z. Shen, *J. Mater. Chem. C*, 2014, **2**, 9689-9694.
48. D. Jiang, L. Li, H. Chen, H. Gao, Q. Qiao, Z. Xu and S. Jiao, *Appl. Phys. Lett.*, 2015, **106**, 171103.
49. X. Xie, Z. Zhang, B. Li, S. Wang, M. Jiang, C. Shan, D. Zhao, H. Chen and D. Shen, *Appl. Phys. Lett.*, 2013, **102**, 231122.
50. O. Katz, V. Garber, B. Meyler, G. Bahir and J. Salzman, *Appl. Phys. Lett.*, 2001, **79**, 1417-1419.
51. Z. L. Wang, *Adv. Mater.*, 2012, **24**, 4632-4646.
52. B. D. Boruah, A. Mukherjee and A. Misra, *Nanotechnology*, 2016, **27**, 095205.
53. X. Xu, J. Hu, Z. Yin and C. Xu, *ACS Appl. Mater. Interfaces*, 2014, **6**, 5983-5987.
54. J. Yu, L. Dong, B. Peng, L. Yuan, Y. Huang, L. Zhang, Y. Zhang and R. Jia, *J. Alloy. Compd.*, 2020, **821**, 153532.
55. S. Li, J. Yue, Z. Yan, Z. Liu, C. Lu, P. Li, D. Guo, Z. Wu, Y. Guo and W. Tang, *J. Alloy. Compd.*, 2022, **902**, 163801.
56. A. S. Pratiyush, S. Krishnamoorthy, S. Kumar, Z. Xia, R. Muralidharan, S. Rajan and D. N. Nath, *Jpn. J. Appl. Phys.*, 2018, **57**, 060313.
57. Y.-C. Chen, Y.-J. Lu, C.-N. Lin, Y.-Z. Tian, C.-J. Gao, L. Dong and C.-X. Shan, *J. Mater. Chem. C,* 2018, **6**, 5727-5732.
58. C. Wu, L. Qiu, S. Li, D. Guo, P. Li, S. Wang, P. Du, Z. Chen, A. Liu and X. Wang, *Mater. Today Phys.*, 2021, **17**, 100335.
59. J. Zhang, S. Jiao, D. Wang, S. Gao, J. Wang and L. Zhao, *Appl. Surf. Sci.*, 2021, **541**, 148380.

